JACS
JOURNAL OF THE AMERICAN CHEMICAL SOCIETY
Article
pubs.acs.org/JACS

Rutile-TiO_2 Nanocoating for a High-Rate $Li_4Ti_5O_{12}$ Anode of a Lithium-Ion Battery

Yong-Qing Wang,[†] Lin Gu,[‡,§] Yu-Guo Guo,*[,†] Hong Li,[‡] Xiao-Qing He,[‡] Susumu Tsukimoto,[§] Yuichi Ikuhara,[§,⊥,∥] and Li-Jun Wan*[,†]

[†]Beijing National Laboratory for Molecular Sciences (BNLMS), Institute of Chemistry, Chinese Academy of Sciences (CAS), Beijing 100190, People's Republic of China

[‡]Beijing National Laboratory for Condensed Matter Physics, Institute of Physics, CAS, Beijing 100190, People's Republic of China

[§]WPI Advanced Institute for Materials Research, Tohoku University, Sendai 980 8577, Japan

[⊥]Nanostructures Research Laboratory, Japan Fine Ceramic Centre, Nagoya, 456-8587, Japan

[∥]Institute of Engineering Innovation, the University of Tokyo, Tokyo, 113-8656, Japan

Supporting Information

ABSTRACT: Well-defined $Li_4Ti_5O_{12}$ nanosheets terminated with rutile-TiO_2 at the edges were synthesized by a facile solution-based method and revealed directly at atomic resolution by an advanced spherical aberration imaging technique. The rutile-TiO_2 terminated $Li_4Ti_5O_{12}$ nanosheets show much improved rate capability and specific capacity compared with pure $Li_4Ti_5O_{12}$ nanosheets when used as anode materials for lithium ion batteries. The results here give clear evidence of the utility of rutile-TiO_2 as a carbon-free coating layer to improve the kinetics of $Li_4Ti_5O_{12}$ toward fast lithium insertion/extraction. The carbon-free nanocoating of rutile-TiO_2 is highly effective in improving the electrochemical properties of $Li_4Ti_5O_{12}$, promising advanced batteries with high volumetric energy density, high surface stability, and long cycle life compared with the commonly used carbon nanocoating in electrode materials.

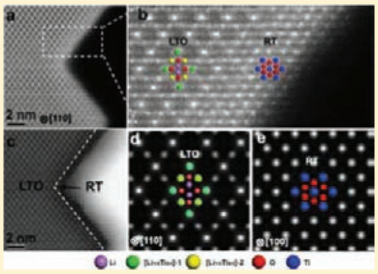

INTRODUCTION

The current interests in the development of more efficient and convenient methods for utilization of our energy resources have prompted the study of a series of intercalation compounds for advanced electrochemical energy storage devices such as lithium ion batteries.[1−4] Among the candidates, spinel $Li_4Ti_5O_{12}$ has attracted considerable attention because of its intrinsic characteristics.[5−11] On one hand, it has a higher Li-insertion voltage (ca. 1.5 V vs Li^+/Li) than that of commercial graphite anode (below 0.2 V vs Li^+/Li), which can avoid reduction of electrolyte on the surface of the electrode and formation of the solid-electrolyte interphase (SEI) layer (usually occurring below 1.0 V Li^+/Li).[12,13] On the other hand, spinel $Li_4Ti_5O_{12}$ is a zero-strain insertion material, which has excellent reversibility toward lithium insertion/extraction.[14−16] These two features make it a promising anode material for lithium ion batteries used in the fields of hybrid electric vehicles and large-scale energy storage, in which long cycle life, high safety, and high power density are highly desired. Despite that, the former two requirements are well met for spinel $Li_4Ti_5O_{12}$, the achievement of the latter is hindered by its kinetic problems with low electrical conductivity (ca. 10^{-13} S cm^{-1}) and lithium diffusion coefficient (ca. 10^{-9} to 10^{-13} cm^2 s^{-1}).[17,18]

So far, many strategies have been reported for enhancing the rate capability of $Li_4Ti_5O_{12}$, which include doping with foreign atoms and using nanostructures and electronically conductive coatings.[19−28] $Li_4Ti_5O_{12}$ nanostructures with electronically conductive coating layers on the surface appear to be more efficient for improving the high rate capability, because the transport lengths of both lithium ions and electrons are significantly shortened. A successful example of the strategies is the well-known carbon-based coating technique. However, because of safety issues concerning carbon materials, great efforts are also directed to carbon-free coatings for achieving superior rate performance, high tap density, and surface stability. Two recently reported carbon-free coatings intended for improving the rate performance of $Li_4Ti_5O_{12}$ may be mentioned in this context: (1) the use of TiN as nanocoating layer;[28] (2) the use of anatase TiO_2.[29] Both designs lead to enhanced rate performance, but the anatase TiO_2 in the latter case is not a well-defined coating layer but an admixture. At this stage, a novel $Li_4Ti_5O_{12}$ nanostructure with favorable morphology for lithium ion transport and uniform carbon-free conducting nanocoating layer and its facile synthesis are still highly desired.

Here, we report a one-pot hydrothermal synthesis process for the fabrication of $Li_4Ti_5O_{12}$ nanosheets and the epitaxial growth of a nanocoating of well-crystallized rutile-TiO_2 at the edges of the nanosheets for the first time. Benefiting from the two-dimensional (2D) nanostructure with large contact surface

Received: February 8, 2012
Published: April 24, 2012

dx.doi.org/10.1021/ja301266w | *J. Am. Chem. Soc.* 2012, 134, 7874−7879

areas with the electrolyte and significantly shortened transport lengths of lithium ions, the as-prepared $Li_4Ti_5O_{12}$ nanosheets (LTO NSs) show superior electrochemical performances in terms of specific capacity, cycling performance, and rate performance, when used as anode materials for lithium ion batteries. The $Li_4Ti_5O_{12}$ nanosheets terminated with rutile-TiO_2 exhibit much improved rate capability compared with pristine LTO NSs. This finding indicates the feasibility of modifying $Li_4Ti_5O_{12}$ through tuning surface termination through facile one-pot synthesis instead of commonly applied complicated coating procedures.

■ EXPERIMENTAL SECTION

Synthesis. The LTO NSs were synthesized using a one-pot hydrothermal procedure. Typically, 1.7 mL (5 mM) of tetrabutyltitanate (TBT) and 0.189 g (4.5 mM) of $LiOH·H_2O$ (Aldrich) were thoroughly mixed in 25 mL of ethanol at ambient temperature. The solution was mixed completely using a magnetic stirrer in a closed container placed in dry environment for about 12 h so as to avoid hydrolysis of TBT with moisture before LiOH dissolved in ethanol. Water (25 mL) was added to the container, and the mixture was kept strongly stirring for 1 min. Then the ivory solution was transferred to a 100 mL Teflon-lined stainless autoclave and was placed in an oven at 180 °C for 36 h. The powder deposited at the bottom of the reactor was collected, washed with ethanol three times, and then dried in oven at 80 °C for 6 h. To form the LTO NSs, the precursor was heated at 500, 600, and 700 °C for 6 h in a horizontal tube furnace in air.

Structural Characterization. The size and morphology of the LTO NSs were characterized using a JEOL 6701F scanning electron microscope (SEM) operated at 10 kV. High-resolution transmission electron microscopy (HRTEM) was performed using a Tecnai G2 20S-TWIN transmission electron microscope (TEM) operated at an accelerating voltage of 200 kV. High-angle annular-dark-field (HAADF) and annular-bright-field (ABF) imaging was executed using a JEOL 2100F (JEOL, Tokyo, Japan) scanning transmission electron microscope (STEM) operated at 200 kV with a CEOS hexapole Cs corrector (CEOS GmbH, Heidelberg, Germany) to cope with the probe forming objective spherical aberration. The phase and the crystallographic structure of the NSs were characterized by powder X-ray diffraction (XRD) using a Regaku D/Max-2500 diffractometer equipped with a Cu $K\alpha_1$ radiation (λ = 1.54056 Å).

Electrochemical Characterization. Electrochemical measurements were performed using Swagelok-type cells assembled in an argon-filled glovebox. For preparing the working electrode, a mixture of LTO NSs, super-P (SP), and poly(vinyl difluoride) (PVDF, Aldrich) at a weight ratio of 80:10:10 was pasted on a pure Cu foil (99.6%, Goodfellow). The loading mass of active materials is about 10 mg cm^{-2}, and the tap density of the material is about 1.5 g cm^{-3}. Pure lithium foil was used as a counter electrode. A glass fiber (GF/D) from Whatman was used as a separator. The electrolyte consisted of a solution of 1 M $LiPF_6$ in ethylene carbonate (EC)/dimethyl carbonate (DMC)/diethyl carbonate (DEC) (1:1:1, in wt %) obtained from Tianjin Jinniu Power Sources Material Co., Ltd. Galvanostatic tests of the assembled cells were carried out using an Arbin BT2000 system in the voltage range of 1.0−2.5 V (vs Li^+/Li). The specific capacities were calculated based on the total mass of active materials including LTO and rutile-TiO_2.

■ RESULTS AND DISCUSSION

Figure 1 shows the X-ray diffraction (XRD) patterns of two as-obtained samples synthesized with different Li/Ti molar ratios and calcinated at 500 °C for 6 h in air. It is found that the phase purity of the products strongly depends on the molar ratio of Li/Ti. With a ratio of 4.5:5, phase-pure $Li_4Ti_5O_{12}$ was obtained in the final product, as demonstrated by all peaks in the XRD pattern of the product (Figure 1a) being well indexed as spinel $Li_4Ti_5O_{12}$ (JCPDS Card No. 49-0207, space group $Fd\bar{3}m$(227), a = 8.36 Å). The sample is denoted as LTO-500. Note that the XRD pattern of the as-prepared precursor indicates that the hydrothermal product is orthorhombic $(Li_{1.81}H_{0.19})Ti_2O_5·2H_2O$ (Figure S1 in Supporting Information). During calcination at elevated temperature, the $(Li_{1.81}H_{0.19})Ti_2O_5·2H_2O$ precursor converts to spinel $Li_4Ti_5O_{12}$.

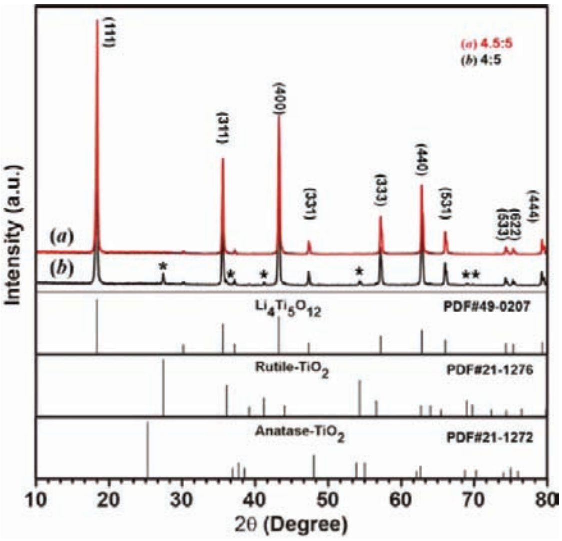

Figure 1. XRD patterns of the as-prepared LTO NSs synthesized with different Li/Ti molar ratios: (a) 4.5:5; (b) 4:5. The ∗ denote the XRD peaks of rutile-TiO_2. Both samples were obtained after calcination at 500 °C for 6 h in air.

Rutile-TiO_2 appears in the final products when the ratio is 4:5 (Figure 1b). No diffraction peak of anatase-TiO_2 is found in the XRD pattern. In the case of calcination at 600 and 700 °C, a similar trend is found on the effect of Li/Ti molar ratio on the composition of final products. When the Li/Ti ratio is 4.5:5, the XRD patterns of the products (denoted as LTO-600 and LTO-700) exhibit a pure LTO phase with improved crystallinity compared with LTO-500. Slightly enhanced XRD peaks corresponding to rutile-TiO_2 are found in the LTO products synthesized with a Li/Ti molar ratio of 4:5 (Figures S2 and S3 in Supporting Information). The results here indicate that the Li/Ti molar ratio has an influence on the chemical composition of the final products. The size and morphology of the LTO-based products were characterized by transmission electron microscopy (TEM) and scanning electron microscopy (SEM). All samples here were prepared with a Li/Ti molar ratio of 4.5:5. Figure 2a shows the typical SEM images of the $(Li_{1.81}H_{0.19})Ti_2O_5·2H_2O$ precursor before calcination. The SEM image clearly shows that the products are 2D NSs with a submicrometer diameter and a mean thickness less than 10 nm, which is further confirmed by AFM measurement (Figure S4 in Supporting Information). After calcination at 500 °C for 1 h, the as-obtained LTO NSs remain in the original sheet-like morphology with an increased thickness of about 20−30 nm and a decreased diameter compared with the precursor, as shown in Figure 2b. When they are calcined at a higher temperature such as 600 °C for 1 h, the thickness of the NSs increases to about 30−60 nm with a stacked NS morphology (Figure 2d). In the case of 700 °C calcination, the thickness even increases to about 50−80 nm. The results clearly indicate that calcination temperature significantly influences the thickness of NSs. The higher the calcination temperature is, the thicker NSs are.

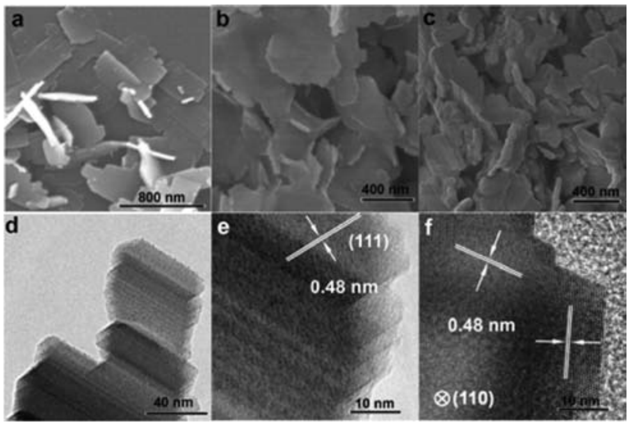

Figure 2. Morphology and structure: (a) SEM image of $(Li_{1.81}H_{0.19})$-$Ti_2O_5{\cdot}2H_2O$ precursor prepared with a Li/Ti ratio of 4.5:5. SEM images of LTO NSs obtained after calcination at (b) 500 °C and (c) 700 °C for 1 h. TEM images of LTO NSs obtained after calcination at (d, e) 600 °C for 1 h and (f) 500 °C for 3 h.

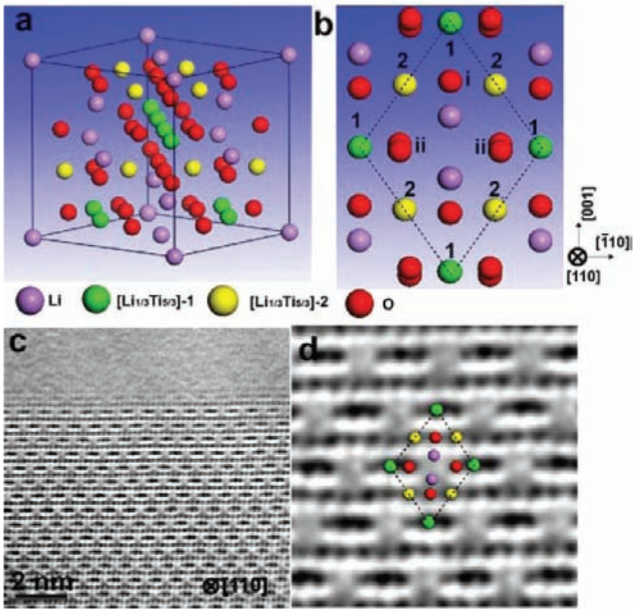

Figure 3. Spinel crystal structure and STEM images of LTO-600: (a) the spinel structure of $Li_4Ti_5O_{12}$ (space group $Fd\bar{3}m$); (b) projection along the [110] direction showing separate Li, O, and $[Li_{1/3}Ti_{5/3}]$ columns. $[Li_{1/3}Ti_{5/3}]$-1 and $[Li_{1/3}Ti_{5/3}]$-2 columns have different atomic densities, and O-ii columns are slightly misaligned. (c, d) ABF images of the as-synthesized LTO-600 NSs.

Figure 2e,f shows the HRTEM images of LTO NSs calcinated at 600 °C for 1 h and 500 °C for 3 h, respectively. The observed and calculated d-spacings from the HRTEM images were 0.48 nm, which matches well with the d-spacing of {111} facets of spinel $Li_4Ti_5O_{12}$. It is worth noting that the NSs synthesized at a low calcination temperature of 500 °C and a short calcination time of 1 h have an unstable structure, which is susceptible to electron beam damage (Figure S5 in Supporting Information). In view of this point, we prefer high calcination temperatures of 600 and 700 °C for the preparation of LTO with high crystallinity. However, as discussed above, at higher calcination temperature, thicker sheets are obtained due to the stack of NSs, which is unfavorable for transportation of Li ions. The best LTO NSs for Li storage need further investigation as described below.

The well-defined structures are visualized directly at atomic resolution by a newly developed aberration-corrected scanning transmission electron microscopy (STEM)[30−33] technique equipped with annular-bright-field (ABF) and high-angle annular-dark-field (HAADF) detectors. Figure 3a shows the spinel structure of LTO. Figure 3b shows the [110] projection of spinel LTO, which is most suitable for observing Li, O, and $[Li_{1/4}Ti_{5/4}]$ atoms directly, because separate columns of these atoms are aligned in this direction. The color spheres in Figure 3a,b represent different atoms, which are marked as $[Li_{1/4}Ti_{5/4}]$, O, and Li atoms, respectively. The $[Li_{1/3}Ti_{5/3}]$ represents $Li_{0.33}Ti_{0.67}$, meaning that Li (or Ti) has 1/3 chance (or 2/3) to occupy octahedral 16d sites in spinel $Li_4Ti_5O_{12}$ lattice. The diameters of the color spheres shown in Figure 3 do not represent the actual sizes of the respective atoms. Eight $[Li_{1/3}Ti_{5/3}]$ columns form a diamond configuration, with two Li atoms at the center. Furthermore, the O atoms in the O-ii columns are slightly misaligned along the [110] direction (Figure 3b), and the number of $[Li_{1/3}Ti_{5/3}]$ atoms in the $[Li_{1/3}Ti_{5/3}]$-1 column is twice that of the $[Li_{1/3}Ti_{5/3}]$-2 columns.[34]

In ABF images, black dots represent atomic positions of atoms, and the contrast is strongly related to the atomic number, following a $Z^{1/3}$ trend. Figure 3c,d shows the ABF images of the as-obtained LTO NSs synthesized with a Li/Ti ratio of 4.5:5 and calcinated at 600 °C for 6 h (i.e., LTO-600). Regular atomic arrangement with a homogeneous surface can be observed in these images, which is consistent with that of the crystal structure of spinel LTO (Figure 3b). The results demonstrate well the crystallinity and high phase purity of the LTO-600 NSs.

Figure 4a−c shows the ABF and HAADF images of LTO NSs synthesized with a Li/Ti molar ratio of 4:5 and calcinated at 600 °C for 6 h (denoted as LTO-RT-600). The HAADF (Figure 4a) and corresponding ABF (Figure 4c) images of the LTO-RT-600 NSs disclose an epitaxial growth thin layer with a thickness of ~1 nm existing at the edge of the NS. The inner part of the LTO-RT-600 has the same atomic arrangement as the simulated HAADF image of LTO projected from the [110]

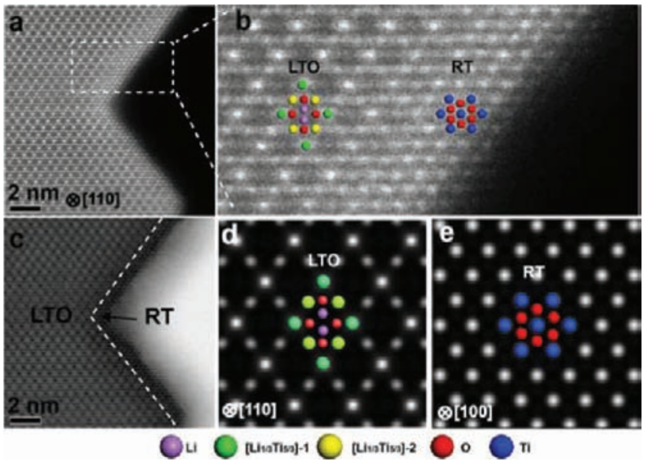

Figure 4. STEM images of LTO-RT-600: (a, b) HAADF and (c) corresponding ABF images of LTO-RT-600 NSs. The simulated HAADF images of (d) LTO projected from [110] direction and (e) rutile-TiO_2 projected from [100] direction. The insets show the arrangements of atoms.

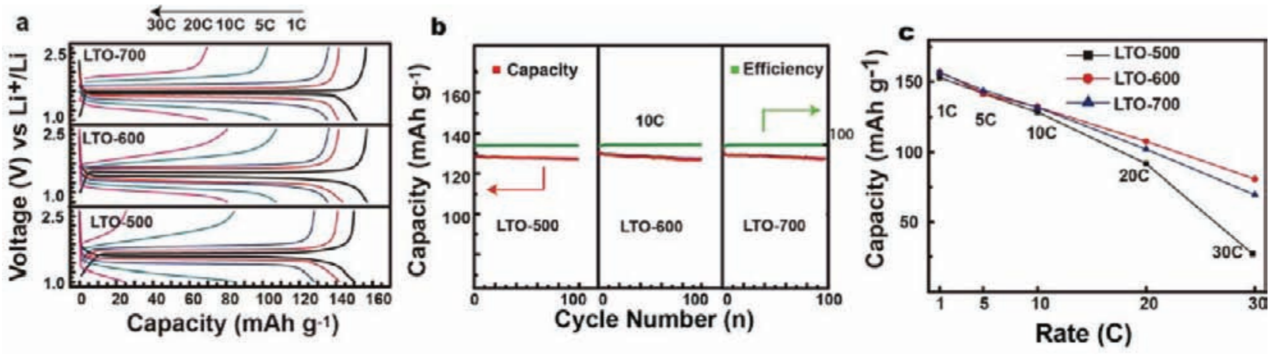

Figure 5. Electrochemical performances of the LTO-500, LTO-600, and LTO-700 NSs: (a) galvanostatic discharge/charge voltage profiles cycled at different rates; (b) cycling performance at 10 C; (c) rate capability.

direction (Figure 4d), while the arrangement at the edge side is quite different. More Ti atoms exist at the edge side than in the inner part, and the arrangement of Ti at the edge is similar to that of the simulated HAADF image of rutile-TiO_2 projected from the [100] direction (Figure 4e). In view of the existence of the XRD peaks of rutile-TiO_2 in the XRD pattern of the sample (Figure S2 in Supporting Information), the edge coating layer is confirmed as rutile-TiO_2 epitaxially grown along its [001] direction. Based on the thickness of the rutile-TiO_2 coating layers and the size of the NSs, the fraction of rutile-TiO_2 is estimated to be ~3.95% in volume and ~4.4% in weight (Figure S6 in Supporting Information).

To test the potential application of the LTO-based NSs in Li ion batteries, we investigated their electrochemical performance toward Li insertion/extraction. Three samples synthesized with the same Li/Ti molar ratio of 4.5:5, but calcinated at different temperatures of 500, 600, and 700 °C (i.e., LTO-500, LTO-600, and LTO-700) were tested. Figure 5 shows the galvanostatic discharge/charge voltage profiles of the three samples cycled at different rates in the voltage range of 1.0−2.5 V vs Li^+/Li. All the samples show a high specific capacity of 145−155 mA h g^{-1} at 1 C and can be operated at 10 C for 100 cycles with slight capacity decay. The results indicate the superiority of LTO-based NSs as high-performance anode materials for Li ion batteries. Among the three samples, the LTO-600 shows the best rate performance. At a high rate of 30 C, it can still deliver a capacity of ca. 80 mA h g^{-1}, while the LTO-700 and the LTO-500 only deliver a capacity of ca. 70 and ca. 25 mA h g^{-1}, respectively. The outstanding performance of the LTO-600 could be attributed to the following aspects: First, in comparison with the LTO-500 NSs, the LTO-600 NSs have high crystallinity. Second, the LTO-600 NSs are thinner than the LTO-700 NSs, which would shorten the transport lengths for Li ions and electrons in NSs.

To address the effect of rutile-TiO_2 on the electrochemical performance of LTO, pure LTO-600 NSs and LTO-RT-600 NSs with a thin rutile-TiO_2 terminated layer at the edges were chosen for comparison studies. Figure 6a displays the discharge/charge voltage profiles of the LTO-RT-600 NSs cycled at various current rates from 1 to 60 C. The corresponding profiles of the LTO-600 NSs refer to Figure 5a. The first discharge specific capacity of the LTO-RT-600 NSs is 178 mA h g^{-1} at 1 C, which is a little higher than the theoretical capacity of $Li_4Ti_5O_{12}$ (175 mA h g^{-1}) owing to capacity contribution from rutile-TiO_2 (336 mA h g^{-1}), and also higher than that of LTO-600 (ca. 155 mA h g^{-1}). The result indicates the enhanced Li electroactivity of LTO-RT-600 NSs after introduction of the rutile-TiO_2 terminal layer. Figure 6b compares the rate capabilities of the LTO-RT-600 NSs and the LTO-600 NSs at different rates. The discharge specific capacities of the LTO-600 NSs decrease significantly from 1 to 60 C, whereas the LTO-RT-600 NSs decrease much more slowly at the same rate. At the highest rate of 60 C, corresponding to a time of 60 s to fully discharge/charge the materials, the LTO-RT-600 still delivers a capacity of 110 mA h g^{-1}, which is much higher than that of LTO-600 (ca. 10 mA h g^{-1}). The reversibility of LTO-RT-600 is demonstrated by the fact that the capacity of 178 mA h g^{-1} is regained when the rate is lowered to 1 C. We are not aware of such a good performance at these high rates in the literature. Especially, the performance at such high rates is much better than that of nanoporous LTO,[8] carbon-coated LTO,[19] TiN-coated LTO,[28] and LTO−graphene and LTO−carbon composites (ca. 83 mA h g^{-1} at 60 C).[7,35]

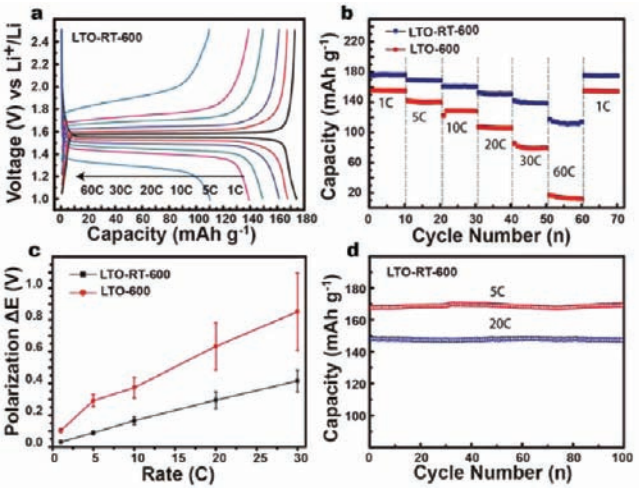

Figure 6. Electrochemical performance of the LTO-RT-600 and LTO-600 NSs: (a) galvanostatic discharge/charge voltage profiles at different rates; (b) rate performance; (c) plots of Δ*E* versus C rates; (d) cycle performance at 5 and 20 C.

The orientation of rutile-TiO_2 at the edge of LTO-RT-600 toward the surface is [100] direction; thus we can easily conclude that rutile-TiO_2 grows along [001] direction, which has a thickness of ~1 nm observed from Figure 4a−c. The highest Li^+ diffusion coefficient (10^{-6} cm^2 s^{-1})[36] is obtained for the [001] direction of rutile-TiO_2; considering the shorter diffusion length along this direction (i.e., the thickness), this epitaxial growth layer is most favorable for fast Li^+ transportation.

Figure 6c shows the polarization of ΔE versus rate plots of the LTO-600 and the LTO-RT-600 electrodes. The values of ΔE are defined as the differences between the potentials of charge plateaus and discharge plateaus. Both plots show nearly a linear dependence with relation to the discharge/charge rates. The linear relationship implies an ohmic behavior of both electrodes at these current densities. The ohmic resistance (R) of both electrodes evaluated from the slope of the fitted line is 84 Ω for the LTO-RT-600 electrode and 122 Ω for the LTO-600 electrode. The smaller R of the LTO-RT-600 electrode could contribute to the improved rate capability.

Another excellent property of the LTO-RT-600 NSs is the superior cycle performance with very slight capacity decay. After 100 discharge/charge cycles at 5 and 20 C, the LTO-RT-600 NSs still deliver a specific capacity of as high as 168 and 149 mA h g^{-1}, respectively (Figure 6c). The LTO-RT-600 NSs were tested in expanded voltage limits of 1.0–3.0 V and 0.7–3.0 V (vs Li^+/Li) to investigate their stability under overcharge and overdischarge conditions. Good cycle performance with slight capacity loss (ca. 2–8%) over 100 cycles is found in both cases (Figure S7 in Supporting Information). The results indicate that the LTO-RT-600 NSs are quite stable under these operating conditions.

To clarify the effects of rutile-TiO_2 coating on the electrochemical properties of LTO, electrochemical impedance spectroscopy (EIS) and potentiostatic intermittent titration technique (PITT) were carried out for both LTO-RT-600 and LTO-600 NSs (Figure S8 in Supporting Information). The EIS results indicate that the charge transfer resistance of LTO-RT-600 is 67 Ω, which is about two times lower than that of LTO-600 (ca. 123 Ω). The PITT results show that apparent chemical diffusion coefficient (D) of lithium in LTO-RT-600 is approximate 4.0×10^{-13} cm^2 s^{-1}, which is much larger than 5.1×10^{-14} cm^2 s^{-1} of LTO-600 NSs. These results clearly indicate that the rutile-TiO_2 nanocoating could improve both the charge transfer reaction and the lithium diffusion coefficient.

The much improved electrochemical performance of the LTO-RT-600 NSs could be attributed to the following aspects: (1) The nanosheet morphology with a thickness of 30–60 nm significantly shortens the diffusion lengths for both Li ions and electrons in the direction perpendicular to the surface of NSs. (2) The rutile-TiO_2 layer does not cover the entire surface of LTO NSs but prefers to epitaxially grow at the edges of the LTO NSs, which inherits the advantage of NS morphology for fast Li ion transportation from liquid electrolyte into the NSs. (3) The rutile-TiO_2 terminal layer at the edges of NSs contributes to the improved kinetics of LTO-RT-600 NSs. On one hand, the epitaxial growth direction of the rutile-TiO_2 layer is along its [001] direction, for rutile-TiO_2, which has the highest Li diffusion coefficient (10^{-6} cm^2 s^{-1}).[36] Therefore, the epitaxial growth layer of rutile-TiO_2 with a tiny thickness of only ~1 nm is favorable for fast Li transportation. On the other hand, it has been reported that anatase TiO_2 in $Li_4Ti_5O_{12}/TiO_2$ could improve the conductivity.[29] Li ions could insert into TiO_2 during the initial discharge process at 1.7 V (vs Li^+/Li), leading to the formation of Li_xTiO_2. The *in situ* formed Li_xTiO_2 is expected to enhance the overall electrical conductivity due to the existence of Ti^{3+}. A similar mechanism might also exist in the LTO-RT-600 NSs. The rutile-TiO_2 could also transfer to Li_xTiO_2 during the initial discharge process with a slope-like profile in the voltage range between 1.55 and 2.5 V (vs Li^+/Li) due to the significant size effect of the rutile-TiO_2 terminal layer with a thickness of ~1 nm.[37] (4) Since nanosized rutile-TiO_2 is also an active Li host with high theoretical capacity (ca. 336 mA h g^{-1}) right in the voltage range used for LTO (1.0–2.5 V vs Li^+/Li),[38] the rutile-TiO_2 coating is superior to traditional carbon coating, which does not show significant Li storage above 1.0 V vs Li^+/Li.

CONCLUSIONS

Lithium ion batteries using carbonaceous anode materials have the risk of safety problems when operating under high current densities as power sources. The carbon-free anode material of $Li_4Ti_5O_{12}$ is a star material to solve the safety issue; however, low kinetics associated with its electrical conductivity limit its high-rate capability in practical applications, and the reported carbon nanocoating strategy again incurs a safety problem. Here we have demonstrated the utility of rutile-TiO_2 as a carbon-free nanocoating to improve the kinetics of $Li_4Ti_5O_{12}$ toward fast lithium insertion/extraction. High-quality LTO-based NSs and rutile-TiO_2-terminated LTO NSs have been synthesized by a facile method through adjusting the molar ratios of starting reactants. These LTO-based NSs exhibit high specific capacities and remarkably high rate capabilities and cycling performances, especially the rutile-TiO_2-terminated LTO NSs, when used as anode materials in Li ion batteries. The carbon-free nanocoating of rutile-TiO_2 not only is proven to be highly effective but also promises high surface stability and long cycle life electrode materials compared with the commonly used carbon nanocoating in electrode materials. The strategy of tuning the surface termination of active material is simple yet very effective because of its versatility, it may also be extended to other anode and cathode materials for future high energy density and high power density Li ion batteries used in electric vehicles and large-scale energy storage. The findings may also trigger interest in studies of the effects of off-stoichiometry on the electrochemical performance of LTO.

ASSOCIATED CONTENT

Supporting Information

XRD patterns of as-prepared NSs before and after calcination at different temperatures, AFM, TEM, and ABF STEM images of NSs, EIS and PITT results of NSs, cycle performance of NSs in expanded voltage limits. This material is available free of charge via the Internet at http://pubs.acs.org.

AUTHOR INFORMATION

Corresponding Author

ygguo@iccas.ac.cn; wanlijun@iccas.ac.cn

Notes

The authors declare no competing financial interest.

ACKNOWLEDGMENTS

This work was supported by the National Basic Research Program of China (Grant Nos. 2012CB932900, 2011CB935700, and 2009CB930400), the National Natural Science Foundation of China (Grant Nos. 91127044, 50730005, and 21121063), and the Chinese Academy of Sciences.

REFERENCES

(1) Tarascon, J. M.; Armand, M. *Nature* **2001**, *414*, 359.

(2) Sun, Y.-K.; Myung, S.-T.; Park, B.-C.; Prakash, J.; Belharouak, I.; Amine, K. *Nat. Mater.* **2009**, *8*, 320.

(3) Cheng, F.; Tao, Z.; Liang, J.; Chen, J. *Chem. Mater.* **2007**, *20*, 667.

(4) Guo, Y.-G.; Hu, J.-S.; Wan, L.-J. *Adv. Mater.* **2008**, *20*, 2878.

(5) Jung, H.-G.; Jang, M. W.; Hassoun, J.; Sun, Y.-K.; Scrosati, B. *Nat. Commun.* **2011**, *2*, 516.

(6) Borghols, W. J. H.; Wagemaker, M.; Lafont, U.; Kelder, E. M.; Mulder, F. M. *J. Am. Chem. Soc.* **2009**, *131*, 17786.

(7) Shen, L.; Yuan, C.; Luo, H.; Zhang, X.; Yang, S.; Lu, X. *Nanoscale* **2011**, *3*, 572.

(8) Shen, L.; Yuan, C.; Luo, H.; Zhang, X.; Xu, K.; Xia, Y. *J. Mater. Chem.* **2010**, *20*, 6998.

(9) Tang, Y. F.; Yang, L.; Qiu, Z.; Huang, J. S. *J. Mater. Chem.* **2009**, *19*, 5980.

(10) Aldon, L.; Kubiak, P.; Womes, M.; Jumas, J.; Olivier-Fourcade, J.; Tirado, J.; Corredor, J.; Vicente, C. P. *Chem. Mater.* **2004**, *16*, 5721.

(11) Sorensen, E. M.; Barry, S. J.; Jung, H.-K.; Rondinelli, J. M.; Vaughey, J. T.; Poeppelmeier, K. R. *Chem. Mater.* **2006**, *18*, 482.

(12) Armand, M.; Tarascon, J. M. *Nature* **2008**, *451*, 652.

(13) Belharouak, I.; Sun, Y. K.; Lu, W.; Amine, K. *J. Electrochem. Soc.* **2007**, *154*, A1083.

(14) Ohzuku, T.; Ueda, A.; Yamamoto, N. *J. Electrochem. Soc.* **1995**, *142*, 1431.

(15) Ariyoshi, K.; Yamato, R.; Ohzuku, T. *Electrochim. Acta* **2005**, *51*, 1125.

(16) Li, H.; Huang, X.; Chen, L.; Zhou, G.; Zhang, Z.; Yu, D.; Mo, Y. J.; Pei, N. *Solid State Ionics* **2000**, *135*, 181.

(17) Wagemaker, M.; van Eck, E. R. H.; Kentgens, A. P. M.; Mulder, F. M. *J. Phys. Chem. B* **2008**, *113*, 224.

(18) Takai, S.; Kamata, M.; Fujine, S.; Yoneda, K.; Kanda, K.; Esaka, T. *Solid State Ionics* **1999**, *123*, 165.

(19) Zhu, G. N.; Liu, H. J.; Zhuang, J. H.; Wang, C. X.; Wang, Y. G.; Xia, Y. Y. *Energy Environ. Sci.* **2011**, *4*, 4016.

(20) Wang, X.-L.; Han, W.-Q.; Chen, H.; Bai, J.; Tyson, T. A.; Yu, X.-Q.; Wang, X.-J.; Yang, X.-Q. *J. Am. Chem. Soc.* **2011**, *133*, 20692.

(21) Zhao, H.; Li, Y.; Zhu, Z.; Lin, J.; Tian, Z.; Wang, R. *Electrochim. Acta* **2008**, *53*, 7079.

(22) Chen, C. H.; Vaughey, J. T.; Jansen, A. N.; Dees, D. W.; Kahaian, A. J.; Goacher, T.; Thackeray, M. M. *J. Electrochem. Soc.* **2001**, *148*, A102.

(23) Zhao, L.; Hu, Y.-S.; Li, H.; Wang, Z.; Chen, L. *Adv. Mater.* **2011**, *23*, 1385.

(24) Wang, G.; Gao, J.; Fu, L.; Zhao, N.; Wu, Y.; Takamura, T. *J. Power Sources* **2007**, *174*, 1109.

(25) Jayaprakash, N.; Moganty, S. S.; Lou, X. W.; Archer, L. A. *Appl. Nanosci.* **2011**, *1*, 7.

(26) Ding, Z.; Zhao, L.; Suo, L.; Jiao, Y.; Meng, S.; Hu, Y. S.; Wang, Z.; Chen, L. *Phys. Chem. Chem. Phys.* **2011**, *13*, 15127.

(27) Nam, K. W.; Wang, X. J.; Yoon, W. S.; Li, H.; Huang, X.; Haas, O.; Bai, J.; Yang, X. Q. *Electrochem. Commun.* **2009**, *11*, 913.

(28) Park, K.-S.; Benayad, A.; Kang, D.-J.; Doo, S.-G. *J. Am. Chem. Soc.* **2008**, *130*, 14930.

(29) Du, G.; Sharma, N.; Peterson, V. K.; Kimpton, J. A.; Jia, D.; Guo, Z. *Adv. Funct. Mater.* **2011**, *21*, 3990.

(30) Huang, R.; Hitosugi, T.; Findlay, S. D.; Fisher, C. A. J.; Ikuhara, Y. H.; Moriwake, H.; Oki, H.; Ikuhara, Y. *Appl. Phys. Lett.* **2011**, *98*, No. 051913.

(31) Gu, L.; Zhu, C.; Li, H.; Yu, Y.; Li, C.; Tsukimoto, S.; Maier, J.; Ikuhara, Y. *J. Am. Chem. Soc.* **2011**, *133*, 4661.

(32) He, X.; Gu, L.; Zhu, C.; Yu, Y.; Li, C.; Hu, Y. S.; Li, H.; Tsukimoto, S.; Maier, J.; Ikuhara, Y. *Mater. Express* **2011**, *1*, 43.

(33) Shao-Horn, Y.; Croguennec, L.; Delmas, C; Nelson, E. C.; O'Keefe, M. A. *Nat. Mater.* **2003**, *2*, 464.

(34) Huang, R.; Ikuhara, Y. H.; Mizoguchi, T.; Findlay, S. D.; Kuwabara, A.; Fisher, C. A. J.; Moriwake, H.; Oki, H.; Hirayama, T.; Ikuhara, Y. *Angew. Chem., Int. Ed.* **2011**, *50*, 3053.

(35) Shen, L.; Yuan, C.; Luo, H.; Zhang, X.; Chen, L.; Li, H. *J. Mater. Chem.* **2011**, *21*, 14414.

(36) Sushko, M. L.; Rosso, K. M.; Liu, J. *J. Phys. Chem. C* **2010**, *114*, 20277.

(37) Cao, F.-F.; Xin, S.; Guo, Y.-G.; Wan, L.-J. *Phys. Chem. Chem. Phys.* **2011**, *13*, 2014.

(38) Hu, Y. S.; Kienle, L.; Guo, Y. G.; Maier, J. *Adv. Mater.* **2006**, *18*, 1421.